AFOSR-TR-97-0644

REPORT DOCUMENTATION PAGE

Form Approved
OMB No. 0704-0188

Public reporting burden for this collection of information is estimated to average 1 hour per response, including the time for reviewing instructions, searching existing data sources, gathering and maintaining the data needed, and completing and reviewing the collection of information. Send comments regarding this burden estimate, or any other aspect of this collection of information, including suggestions for reducing this burden, to Washington Headquarters Services Directorate for Information Operations and Reports, 1215 Jefferson Davis Highway, Suite 1204, Arlington VA 22202-4302, and to the Office of Management and Budget Paperwork Reduction Project (0704-0188), Washington, DC 20503.

1. AGENCY USE ONLY (Leave blank)	2. REPORT DATE 17 Nov. 1997	3. REPORT TYPE AND DATES COVERED Final Technical Report (7/1/94 - 6/30/97)

4. TITLE AND SUBTITLE

A wavelet analysis of mining explosions: Observations relating to verification of a Comprehensive Nuclear Test Ban

5. FUNDING NUMBERS

AFOSR grant 49620-94-1-0410

6. AUTHOR(S)

Michael Hedlin and Deirdre Wendel

7. PERFORMING ORGANIZATION NAME(S) AND ADDRESS(ES)

University of California, San Diego
Scripps Institution of Oceanography
IGPP 0225
La Jolla, CA 92093-0225

8. PERFORMING ORGANIZATION REPORT NUMBER

9. SPONSORING/MONITORING AGENCY NAME(S) AND ADDRESS(ES)

AFOSR/NM
110 Duncan AVe
Room B115
Bolling AFB, MA 20332-8080
ATTN: DR. STANLEY DICKINSON

10. SPONSORING/MONITORING AGENCY REPORT NUMBER

19971203 162

11. SUPPLEMENTARY NOTES

12a. DISTRIBUTION/AVAILABILITY STATEMENT

Approved for public release; distribution unlimited.

12b. DISTRIBUTION CODE

13. ABSTRACT (Maximum 200 words)

International nuclear testing threshold treaties, under effect in some form or another since 1963, have rallied scientists to devise ways of monitoring nuclear weapons tests. The UN General Assembly's adoption of a Comprehensive Test Ban Treaty in 1996 heightens the need to distinguish nuclear events not only from earthquakes, but also from man-made mining explosions. The treaty requires a monitoring threshold potentially as low as magnitude $mg \approx 2.5$ (Stump et al, 1994), which translates to a yield of roughly 16 T of explosive (OTA, 1988). The CTBT is even more stringent than the former international agreement, the Threshold Test Ban Treaty, which already imposed a ceiling of 150 kT (OTA, 1988; personal communication from Dr. Michael Hedlin and Prof. John Orcutt). In the U.S., the number of man-made mining explosions with yield greater than 50 T is about 10,000 per day, about one of which is greater than 200 T (Stump et al, 1994), giving ample justification for a discriminant that sifts earthquakes and nuclear explosions from mining explosions that may occur on the same magnitude scale. What is more, there are various ways to evade the detection of a nuclear test, such as detonating the bomb in an underground cavity or during an earthquake or certain types of mining explosions (OTA, 1988; personal communication from Dr. Michael Hedlin). That evasion tactics can effectively reduce the perceived magnitude by half (OTA, 1988) underscores the need for high-gain, high-confidence identification methods. If testing is to be monitored globally and systematically, it is desirable to differentiate events independently of local testing or mining practices and local geological characteristics. Scientists therefore seek a seismic discriminat.

14. SUBJECT TERMS

CTBT, verification, ripple-firing, wavelets

DTIC QUALITY INSPECTED 3

15. NUMBER OF PAGES
32

16. PRICE CODE

17. SECURITY CLASSIFICATION OF REPORT Unclassified	18. SECURITY CLASSIFICATION OF THIS PAGE Unclassified	19. SECURITY CLASSIFICATION OF ABSTRACT Unclassified	20. LIMITATION OF ABSTRACT SAR

UNIVERSITY OF CALIFORNIA, SAN DIEGO

BERKELEY · DAVIS · IRVINE · LOS ANGELES · RIVERSIDE · SAN DIEGO · SAN FRANCISCO   SANTA BARBARA · SANTA CRUZ

INSTITUTE OF GEOPHYSICS AND PLANETARY PHYSICS
SCRIPPS INSTITUTION OF OCEANOGRAPHY (A-025)
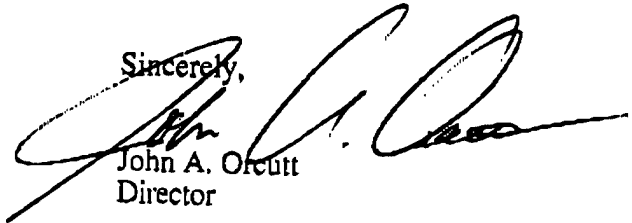FAX: (619) 534-2902

LA JOLLA, CALIFORNIA 92093-0225

11 November 1997

Dr. Stanley Dickinson
Program Manager
AFOSR/NI
ATTN: AASERT Program
110 Duncan Ave., Room B115
Bolling Air Force Base, DC 20332-8050

Dear Dr. Dickinson:

      Enclosed please find a final technical report as well as an AASERT reporting form for our AFOSR grant F49620-94-1-0410 *Hydroacoustic arrays for seismic detection, location and discrimination: A comparison with land-based seismic arrays.* I apologize for the delay in getting this information to you. Please contact me at 619/534-4548 if you have any questions.

Sincerely,

John A. Orcutt
Director

cc: AFOSR/PKA

Chapter 1

Introduction

1.1 Background and Motivation

International nuclear testing threshold treaties, under effect in some form or another since 1963, have rallied scientists to devise ways of monitoring nuclear weapons tests. The UN General Assembly's adoption of a Comprehensive Test Ban Treaty in 1996 heightens the need to distinguish nuclear events not only from earthquakes, but also from man-made mining explosions. The treaty requires a monitoring threshold potentially as low as magnitude $m_b=2.5$ (Stump et al., 1994), which translates to a yield of roughly 16 T of explosive (OTA, 1988). The CTBT is even more stringent than the former international agreement, the Threshold Test Ban Treaty, which already imposed a ceiling of 150 kT (OTA, 1988; personal communication from Dr. Michael Hedlin and Professor John Orcutt). In the U.S., the number of man-made mining explosions with yield greater than 50 T is about 10,000 per day, about one of which is greater than 200 T (Stump et al., 1994), giving ample justification for a discriminant that sifts earthquakes and nuclear explosions from mining explosions that may occur on the same magnitude scale. What is more, there are various ways to evade the detection of a nuclear test, such as detonating the bomb in an underground cavity or during an earthquake or certain types of mining explosions (OTA, 1988; personal communication from Dr. Michael Hedlin). That evasion tactics can effectively reduce the perceived magnitude by half (OTA, 1988) underscores the need for high-gain, high-confidence identification methods. If testing is to be monitored globally and systematically, it is desirable to differentiate events independently of local testing or mining practices and local geological characteristics. Scientists therefore seek a seismic discriminant both highly accurate and highly reproducible, regardless of specific source/receiver setting.

The most prevalent form of mining explosion is what is known as a ripple-fired explosion (Langefors and Kihlstrom, 1978). A ripple-fired explosion consists of a grid of explosive shots that are detonated

sequentially. Michael Hedlin and colleagues have noted that, almost across the board, frequency modulations of high spectral amplitude and long time-duration result from ripple-firing and distinguish these mining events from single-shot explosions. These scientists have also devised a theoretical model and a time and frequency-dependent multitaper transform that successfully reproduce and display the modulation (Hedlin et al., 1989; 1990). This discriminant has the advantage that it appears independently of specific source/receiver setting. However, there are a few cases where it may not appear (Hedlin, 1997).

I have sought to further the analysis by replacing multitapers with the more-refined wavelets, by using phase differences between data components to observe signal polarization, and by extending the analysis to lower frequencies (to between .05 and 1 hz). Until recently, researchers in the seismic verification field have, at best,filtered time series with multitapers, and for many applications this is adequate. Taper transforms provide robust spectral estimates but a limited resolution prescription. Like multitapers, wavelets can be made orthogonal. But unlike multitapers, wavelets provide a flexible trade-off between time and frequency resolution across the time and frequency plane, a feature well-suited to the wide range of energetic frequency content and the closely-spaced arrivals present in seismic signals. By guaranteeing the optimal tradeoff between time and frequency localization, wavelets can resolve simultaneously in time and frequency two pulses both very close in time and very close in frequency, whereas the taper will be limited to resolving the pulses either in time or in frequency (Daubechies, 1987). Therefore, a wavelet can be adjusted to achieve a superior time and frequency resolution tradeoff than a multitaper for a chosen frequency band of interest (the tradeoff will be worse than a taper's elsewhere, but better for the chosen bandwidth). This characteristic is potentially useful for discriminating spectral features in the time and frequency plane, particularly when dealing with regional distances and surface wave spectra, often beset with closely spaced pulses and a great deal of scattered energy. Furthermore, since complex wavelets retain the time and frequency evolution of the relative phase between data recorded along different directions in the earth, we can reconstruct the time and frequency evolution of the signal's polarization. We have shifted the analysis to a lower frequency range with the expectation that some form of time-independent modulation will appear even in those cases where it fails to appear at higher frequencies and even when higher-frequency components have attenuated. Banding in this range stems from finite (as opposed to infinitesimal) source duration. The pattern of signal polarization across the time and frequency plane provides a further constraint upon phase identifications and upon identification of source mechanisms underlying spectral features observed in the time and frequency plane. This may be particularly important for regional and low- to mid-frequency data, again for the reasons mentioned above.

1.2 Thesis organization

The main objective of this thesis is to evaluate results regarding potential distinctions between nuclear and mining explosion spectra, and therefore shall not attempt to cover distinctions between nuclear explosion and earthquake spectra. Since seismic measurements of single-explosion calibration shots at mines are easier to obtain than nuclear explosions, and since ripple-fired mining blasts are the most common form of mining operation, this problem is here recast as a comparison between single calibration shots and ripple-fired quarry shots. I shall therefore begin by describing ripple-firing–what it is, and how it is implemented. It is then necessary to cover the dual time-frequency decomposition known as a sonogram, since this is the rudiment of our tool, and, in so doing, I shall discuss some of the features of ripple-fired mining blasts that sonograms have made observable. Up until now, sonograms have been created with multitaper filters, and so I shall discuss briefly their derivation and important features. More importantly, I will then attempt to provide a summary of the salient properties of wavelets and how, following Lilly and Park (1995), we made use of a wavelet-like filter derived from multitapers. A description of the data sets follows. Based on multitaper and wavelet analyses of a subset of the data, a comparison is then made between the resolution in both cases.

Chapter 3 presents the derivation of the wavelet polarization by way of a singular-value decomposition and a summary of the results simulated from synthetic data. It then introduces samples of results on actual data in order to help assess the tool's validity and usefulness in identifying wavetypes.

Chapter 4 launches a discussion of the low-frequency analysis and some of the most interesting features found there, and some possible ramifications for seismic verification. Particular attention is paid to theoretical underpinnings and evidence for possible differences in surface-wave dispersion in the two explosion types. I discuss the low-frequency results for NRDC and for the Wyoming experiment in relation to this. In the end I try to summarize what has been accomplished and what learned from this exercise, and what remains to be done. I also make suggestions for fruitful future research along these lines.

References

Daubechies, Ingrid, *Orthonormal bases of wavelets with finite support–connection with discrete filters.* Proceedings of the International Colloquium on Wavelets and Applications, Marseille, 1987.

Hedlin, Michael A. H., J. Bernard Minster, and John A. Orcutt, The time-frequency characteristics of quarry blasts and calibration explosions recorded in Kazakhstan, USSR. *Geophys. J. Int.*, **99**, 109-121, 1989.

Hedlin, Michael A. H., J. Bernard Minster, and John A. Orcutt, An automatic means to discriminate between earthquakes and quarry blasts. *Bull. Seismol. Soc. Am.*, **80**, 2143-2160, 1990.

Hedlin, Michael A. H., A global test of a time-frequency small-event discriminant. *submitted, Bull. Seismol. Soc. Am.*, 1997.

Langefors, U. and Kihlström, B., *The modern technique of rock blasting.* Halsted Press, John Wiley and sons, New York, 1978.

Stump, Brian W., Florence Rivière-Barbier, Igor Chernoby, and Karl Koch, Monitoring a test ban treaty presents scientific challenges. *Eos Trans. AGU*, , 265, June 14, 1994.

U.S. Congress, Office of Technology Assessment, *Seismic verification of nuclear testing treaties.* Washington DC., U.S. Government Printing Office, 1988.

Chapter 2

Spectra of single-shot and ripple-fired explosions

2.1 Ripple-firing

Ripple-firing is mining jargon for the common mining technique of fracturing rock with a cascade of explosions. Single explosives are spaced in a generally shallow array of rows and columns on the order of tens of meters apart and detonated sequentially, ideally at regularly-spaced intervals (Figure 2.1). Ripple-firing is an efficient means of loosening large sections of rock while minimizing ground motion and thrown rock (Dowding, 1985). It is the most common form of mining operation worldwide (Langefors and Kihlström, 1978; Stump et al, 1989).

We can model the idealized ripple-fired disturbance $z(t)$ by a finite duration series of impulses each separated by a period T and altogether lasting a time D:

$$z(t) = w(t) * [\frac{III(\frac{t}{T})}{T} B(\frac{t}{D})] \qquad (2.1)$$

where $w(t)$, the basic waveform, is convolved with the finite shah function to simulate repetition, and the shah function III is made finite by the boxcar function B. In real life, however, the time interval between shots strays from the extrapolated regular values. For example, projected and actual shot times can, in parts of the U.S., deviate by up to 34% (Hedlin et al., 1989). For this more general case, we may write

$$z(t) = \sum_j w(t - \delta T_j) \qquad (2.2)$$

where δT_j gives the time of the jth shot relative to the time of the first shot and which can include any deviations from a standard time offset T.

If the shots occur in a spatial array, as is often the case, as in Figure 2.1, we can incorporate the
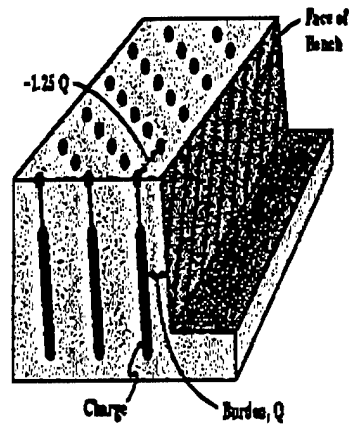
Figure 2.1 A cross-sectional diagram of a typical shot array for a ripple-fired mining explosion. Credit: Dr. Michael Hedlin, IGPP-SIO.

contributions made to the apparent shot interval by the differences in distance between each shot and the receiver. Assuming an absence of shot-time irregularities, we can separate apparent offset times from actual offset times by using the expression

$$\delta T_j^a = p(\delta x_j \sin\theta + \delta y_j \cos\theta) \tag{2.3}$$

where θ is the source to receiver azimuth, p is the horizontal slowness, and δx_j and δy_j are the actual x and y spatial offsets of the shots in the array (see Figure 2.2) (Hedlin et al.,1990; Smith, 1989).

2.2 Spectra of ripple-fired explosions

The Fourier power spectrum reveals time-independent frequency modulation. Reamer, et al. (1992) has shown experimentally that linear superpositioning of shots is more than sufficient to explain amplitude modulations in the observations, even though there has been evidence that it may be necessary to include non-linear interactions between sources in the elastic (very near-source) region (Reamer et al., 1992). The long life of the modulations stems from the protraction of the event: the panoply of wavetrains and their scattered waves that arrive from one shot continue to also arrive from all the shots. It is possible to infer the intershot times from the bandwidth of the lobe spacing, though irregularities in time offset often obscure this relationship. The Fourier transform of expression 2.2 gives

$$\tilde{X}(f) = FT[\sum_j w(t - \delta T_j)] \tag{2.4}$$

$$\left|\tilde{X}(f)\right|^2 = \left|\sum_j FT[w(t)]e^{2\pi i f \delta T_j}\right|^2 = \left|\tilde{W}(f)\sum_j e^{2\pi i f \delta T_j}\right|^2 \tag{2.5}$$

and the power spectrum is

$$P(f) = \left|\tilde{W}(f)\right|^2[(\sum_j \sin 2\pi f \delta T_j)^2 + (\sum_j \cos 2\pi f \delta T_j)^2] \tag{2.6}$$

(Hedlin et al., 1989; 1990). The factor of sines and cosines gives rise to the observed spectral modulations, as shown in Figure 2.3. Figure 2.4 shows the spectrum from a synthetic of 50 shots with randomized time offsets of mean 63 ms and variance 6.3 ms (Hedlin et al., 1989). Figure 2.5, on the other hand, results from a synthetic of 39 cospatial shots spaced at regular time intervals of 25 ms (Hedlin et al, 1990). Because in the latter example there is a clean relationship between offset interval and lobe spacing, we are able to deduce from the lobe spacing of 40 hz (where the boxcar's transform, i.e.the sinc function, has its peaks) a shot interval of 25 ms, or $1/40\ hz^{-1}$. From the widths of the side lobes we are able to deduce the duration of .975 s of the entire blast. The former example still displays a strong frequency modulation at the expected frequencies that are multiples of $1/63\ ms^{-1}$, i.e., 16, 32 and 48 hz, but now the scatter begins to obscure the peaks at the higher overtones. Changes in apparent offset time due to spatial offsets in an array only exacerbate the effects of the scatter and can introduce modulation into the lobes that makes it possible to incorrectly infer the shot intervals. (This is demonstrated in the synthetic spectrum in Figure 2.6, for example, from which we would infer a shot spacing of 170 $ms \approx 1/6\ hz^{-1}$, but for which in fact the *whole set* of shots lasts 384 $ms \approx 1/(2.6)\ hz^{-1}$. The difference in travel times helps reinforce the side lobes.) In fact it has been speculated that most of the modulation we witness in the spectra are not in fact due to the ripple-firing per se, but to the finite (as opposed to infinitesimal) event duration (Hedlin et al., 1990).

2.3 Sonograms

In order to observe the time-independence of the modulation, it is necessary to create a time and frequency-dependent spectrum, known as a sonogram. This is done by taking the discrete Fourier transform of windows of the time series that are staggered in time, which serves to preserve information in time. From the result we compose a matrix whose elements are the series' windowed power spectrum at each time and frequency point (Hedlin et al., 1989, 1990). Since multi-tapers are generated in the same manner as I will show below in the description of wavelets (Park, 1987), I will omit that derivation here. An example of time-independent banding is displayed in Figure 2.7, a sonogram calculated for a Soviet quarry blast.
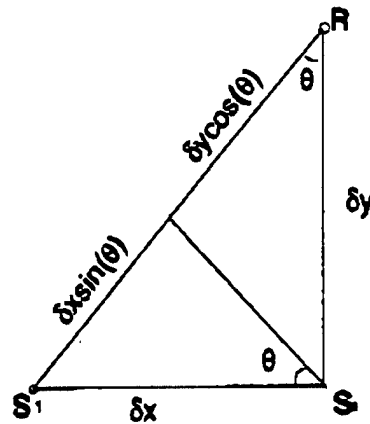
Figure 2.2 The geometry for calculating array spatial offsets as they affect the source-receiver distance function and hence travel time.

Hedlin et al. ruled out a source/receiver origin (e.g., a resonance layer) of the modulation by comparing data from different source types measured at the same station and data from the same event measured at different stations. The effect was also observed in Norway from Norwegian mining blasts, so that it appears region-independent (Hedlin et al., 1990). To help isolate the fundamental spectral patterns from fluctuating amplitude information, Hedlin et al. have reduced the sonogram to a binary sonogram. In this form, the difference between a highly smoothed (convolved with boxcar of width 2.5 hz) and a less-well-smoothed (convolved with a boxcar of width 1. hz) version of the original spectrum is flattened out,,: values above and below the local average are assigned values of +1 and -1, respectively (Hedlin et al., 1989; 1990). The binary sonogram corresponding to Figure 2.7 is shown in Figure 2.8.

2.4 Filtering, multitapers, and wavelets

In this research we have sought to exploit some of the advantages wavelets confer upon multi-dimensional transforms of data. A two-dimensional wavelet transform of a time series provides improved tradeoff between time and frequency resolution. A wavelet transform is therefore particularly advantageous in the analysis of waveforms frought with abrupt changes in time or with narrow, highly-energetic bandwidths, common features of seismic waveforms. Unlike the Fourier transform, the wavelet transform does not restrict the tradeoff between time and frequency localization by fixing the time window (Rioul and Vetterli, 1991; Hlawatsch and Boudreaux-Bartels, 1992; Lilly and Park, 1995; Chakraborty and Okaya, 1995). Instead it allows inversely-varying time and frequency resolutions as it traverses the time series and therefore negotiates the best time-frequency resolution for the time-frequency region of interest. We use
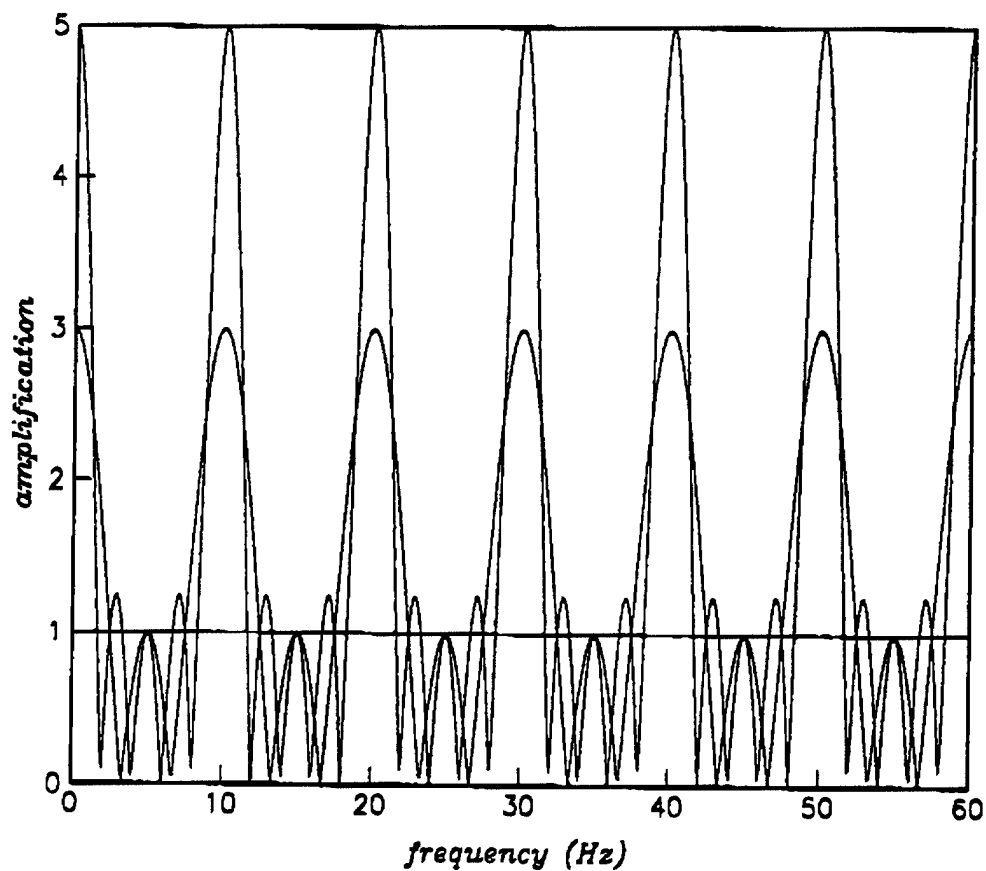
Figure 2.3 Spectrum of linear superposition of 1 to 5 subshots at the same location in space but separated by 100 *ms* from one another. This intershot delay yields modulations spaced every 10 *hz*. Credit: Dr. Michael Hedlin, IGPP-SIO

the wavelets championed by Lilly and Park, which establish a four-fold advantage: while maintaining the resolution properties of classical wavelets, they comprise a set of independent estimates that can be averaged to reduce variance; at the same time, they mimic the spectral-leakage minimization of multitapers without increasing bias (Lilly and Park, 1995).

The classical wavelet is defined to be one member of the set of self-similar, translated, and rescaled versions of a generic mother wavelet whose form is chosen to best window the given time series (see Chakraborty, and Okaya, 1995, to learn how this is done). If the mother wavelet in continuous time is $g(t)$, then the discrete-time wavelets used to convolve the time-series are the set

$$g_{m-b}^a = c_a g(\frac{t-b}{a})$$

(2.7)

with $t = mdt, m = -\frac{M}{2}, \cdots, 0, \cdots, \frac{M}{2}$. Their convolution with the time series s is then given by

$$\tilde{s}(a,b) = \sum_m g_m^a s_{b-m}$$

(2.8)

Here a is the scale parameter, b a time translation parameter proportional to a, and c an amplitude factor dependent on a. dt is the sampling interval. The choice of a sets the time scale of the decomposition (a feature that is mirrored in b's proportionality to a): larger scales a (and hence longer wavelets) canvass larger time intervals, thus revealing more global, large-scale features of the signal, and vice versa, smaller scales inspect the signal more microscopically (Hlawatsch and Boudreaux-Bartels, 1992; Rioul and Vetterli, 1991). a is also proportional to the center frequency f_o of the analyzing wavelet and inversely proportional to f_c, the target frequency in the signal, i.e., $a = f_o/f_c$ (Hlawatsch and Boudreaux-Bartels, 1992). In practice, discrete wavelets are usually generated by applying a filter bank to a time series. The scale parameter a is then defined as a_o^j, j a member of the set of integers (Chakraborty and Okaya, 1995).

If ΔT is the time window, then $\Delta T = Mdt$, where M is an integer. ΔT therefore satisfies the uncertainty relation $\Delta T f_u = (Mdt)f_u = p$, where the constant p is the time-bandwidth product. The so-called time-bandcenter product $p_c = f_c Mdt$ is also a constant. Therefore, $\frac{f_u}{f_c} = p/p_c = $ a constant (Hlawatsch and Boudreaux-Bartels, 1992; Rioul and Vetterli, 1991; Lilly and Park, 1995). This shows that the width of the time window varies inversely to the width of the frequency band, which in turn varies proportionally to f_c. Thus we obtain good frequency resolution at low to mid frequencies, but poor frequency resolution at high frequencies, and likewise, good time resolution at high frequencies, poor time resolution at low frequencies. We can adjust the scale to accomodate time and frequency localization of waves containing sudden, short-lived variation in time or containing narrow energetic bandwidths (Lilly
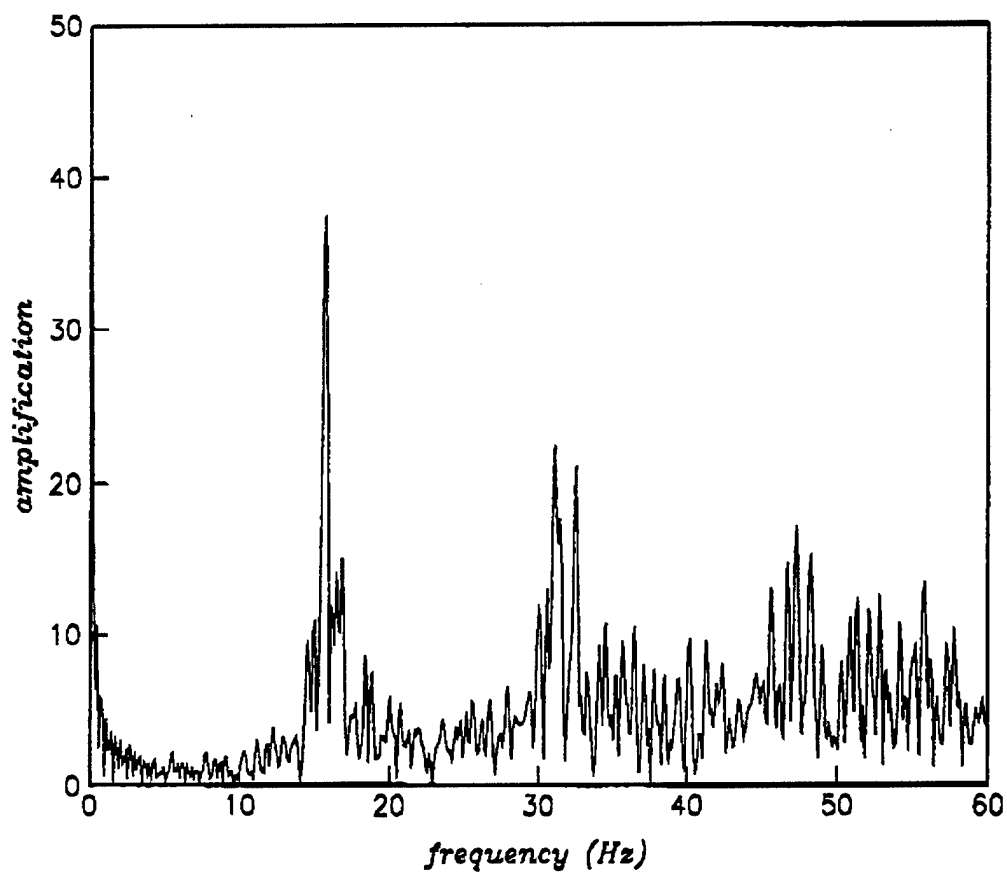
Figure 2.4 Spectrum of synthetic of 50 shots of randomized time offsets of mean 63 *ms* and variance 6.3 *ms*. Credit: Dr. Micale Hedlin, IGPP-SIO.
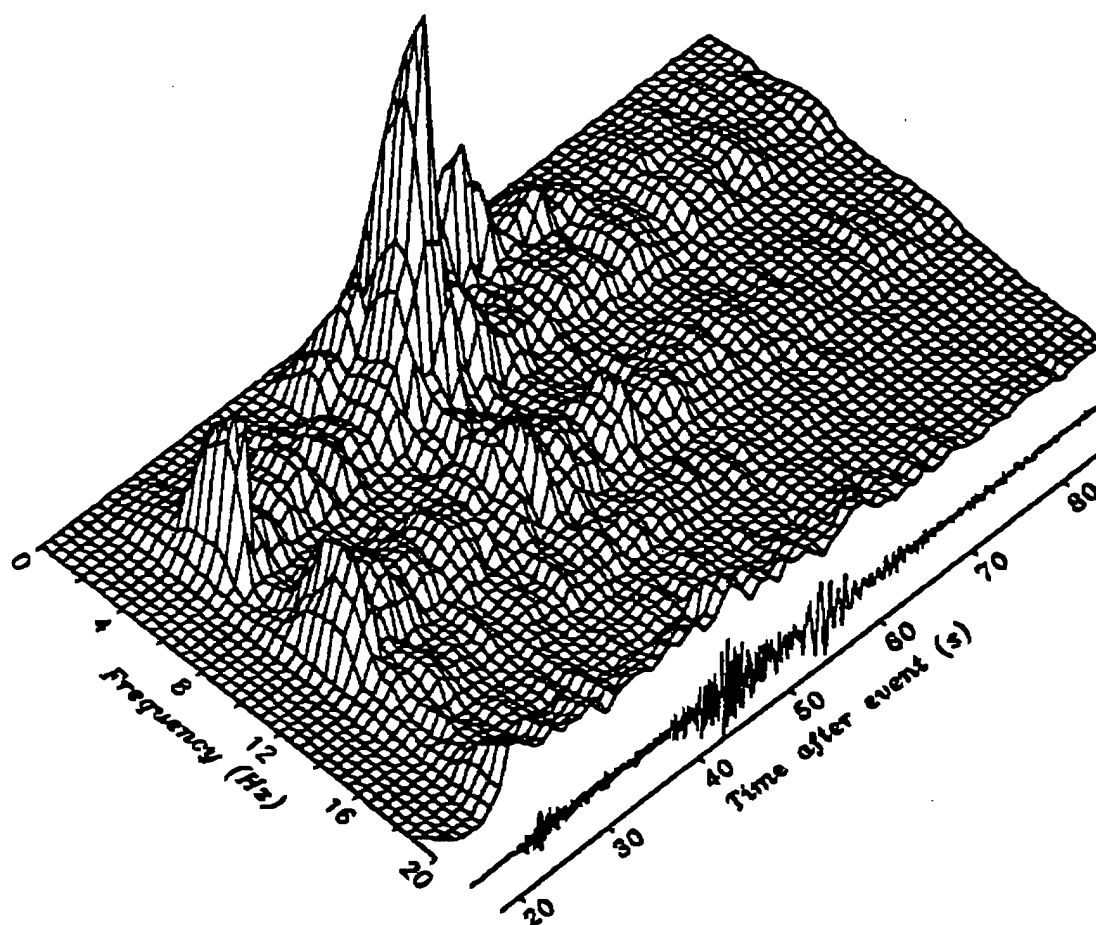
Figure 2.5 Spectrum from synthetic consisting of 39 cospatial shots spaced at regular time intervals of 25 *ms*; the Green's function for this synthetic is the single calibration explosion Chemex 2 examined in this paper. Credit: Hedlin, 1991.

and Park, 1995). Figure 2.9 bears witness to the difference between the time-frequency resolution of a Fourier spectrum and that of a wavelet transform. Fourier and wavelet decompositions are both applied to the function $\delta(t - t_1) + \delta(t - t_2) + exp(i2\pi f_1 t) + exp(i2\pi f_2 t)$, which in effect images the resolving power of each filter in both the time and frequency domains. The top figure illustrates the Fourier resolution, and the bottom figure the wavelet resolution. Apparent are the fixed relationship between time and frequency resolution in the Fourier transform, and the flexible tradeoff between time and frequency resolution across the time-frequency plane in the wavelet transform. Notice the wavelets' improved time resolution at high frequencies and improved frequency resolution at low frequencies (Hlawatsch and Boudreaux-Bartels, 1992).

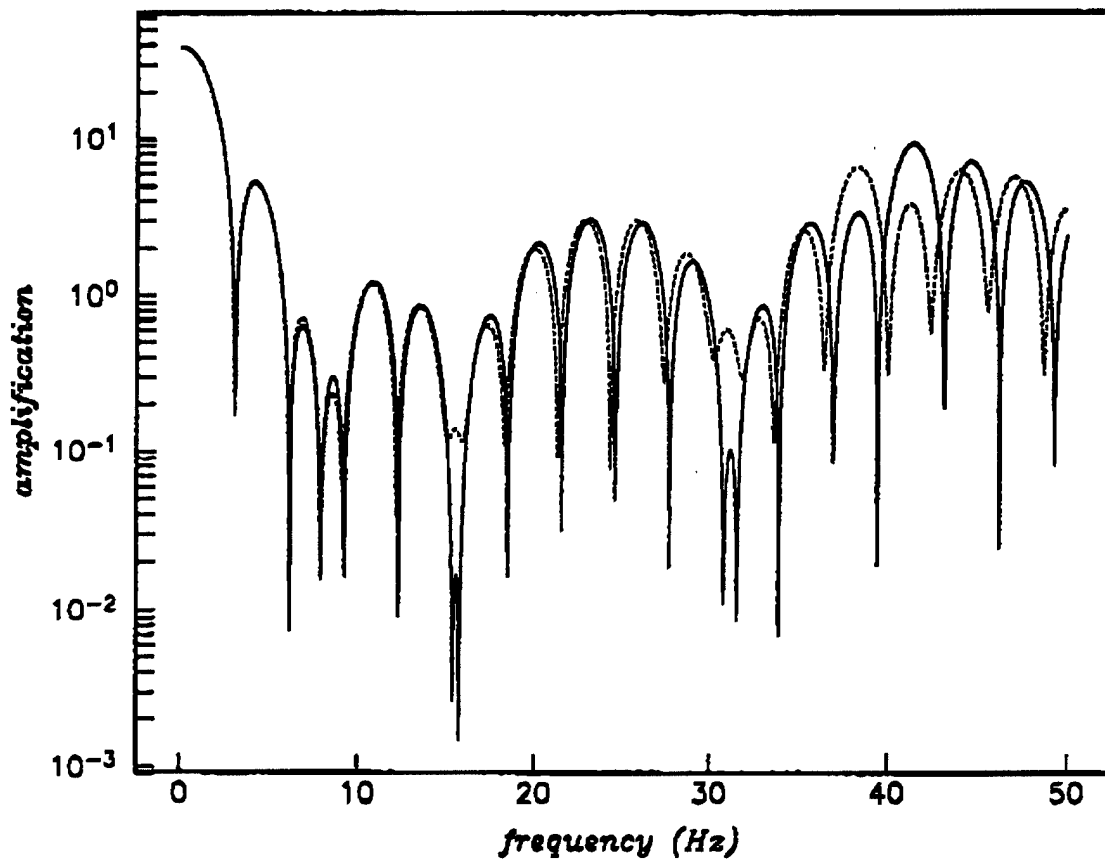We adopt Lilly and Park's method of constructing the basis wavelets by solving the eigenvalue

Figure 2.6 A spectrum demonstrating changes introduced into modulation intervals by spatial offsets between shots in an array. Credit: Hedlin, 1991.

equation maximizing the wavelets' energy spectrum within the chosen bandwidth. Like them, we will also prescribe the parameters p, f_c, and p_e instead of the parameters a, b, and M. If $\{w_m\}$ are the desired wavelet functions, then

$$W(f) = \sum_{m=-M/2+1}^{M/2} w_m e^{2\pi i f m} \tag{2.9}$$

where $|f| \leq \frac{1}{2dt}$, f_c is the target frequency, and $|f - f_c| \leq f_w$. We want to maximize the ratio

$$\lambda(M, f_c, f_w) = \frac{\int_{f_c-f_w}^{f_c+f_w} |W(f)|^2 df + \int_{-f_c-f_w}^{-f_c+f_w} |W(f)|^2 df}{\int_{-1/2}^{1/2} |W(f)|^2 df} \tag{2.10}$$

This is equivalent to the eigenvalue equation

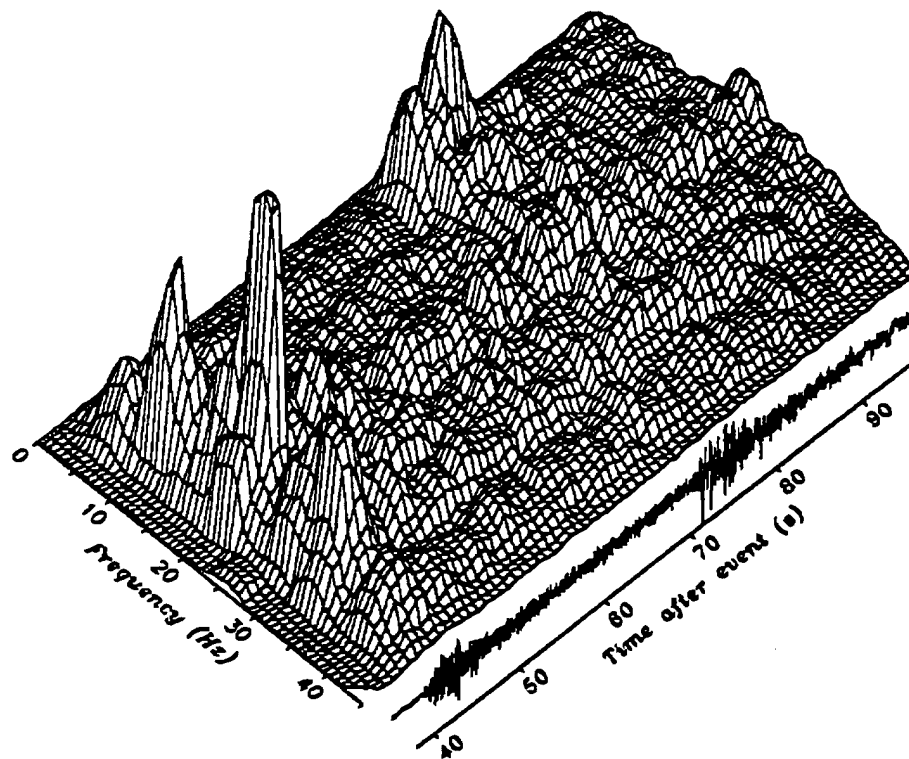$$(C^+ - C^-)x - \lambda x = 0 \tag{2.11}$$

Figure 2.7 Sonogram showing regular, time-independent modulations along the frequency domain; the event is the Soviet quarry blast examined in this paper. Credit: Dr. Michael Hedlin, IGPP-SIO.
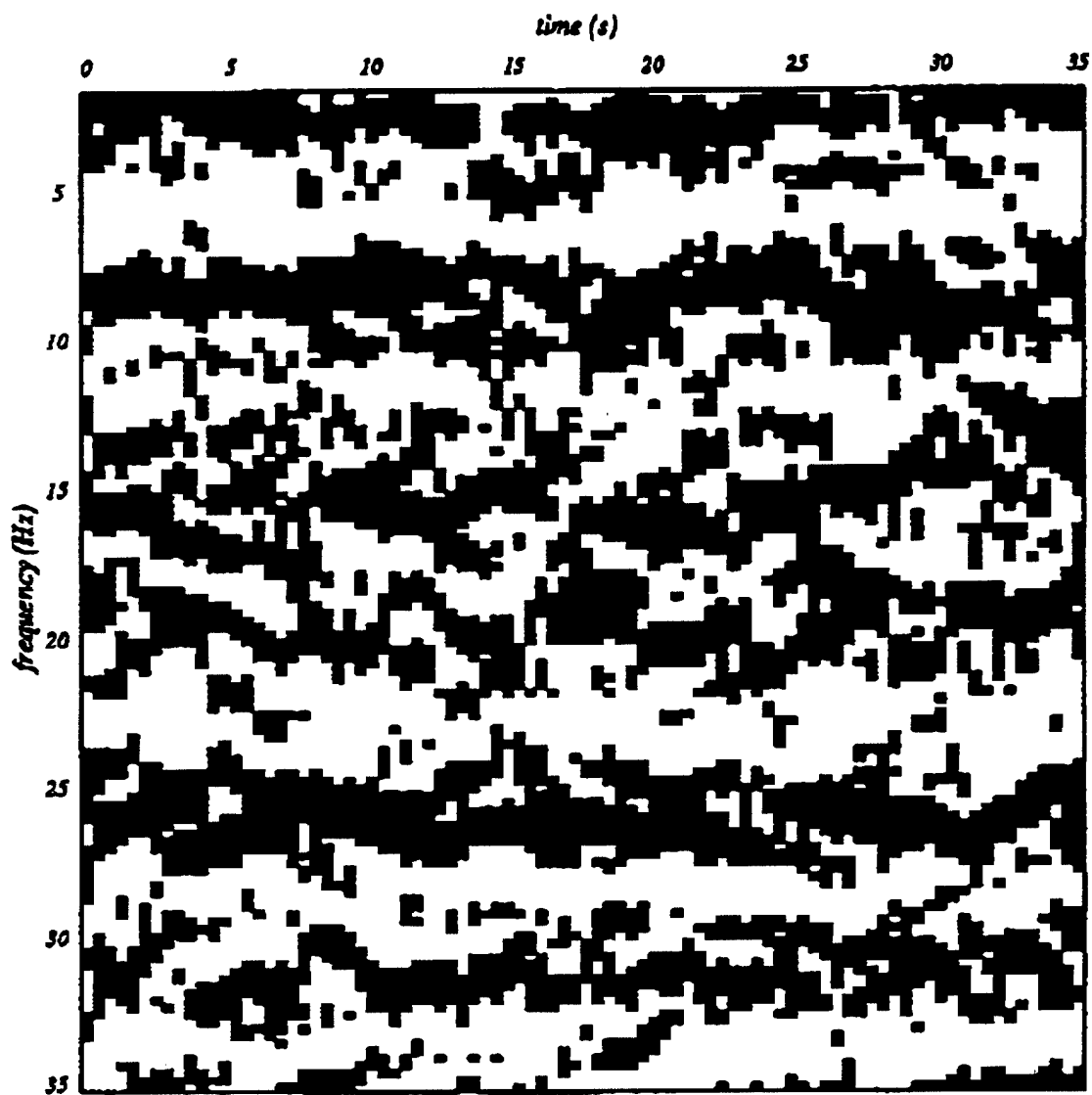
Figure 2.8 Binary sonogram of the same Soviet quarry blast presented in Figure 2.7.

Credit: Hedlin, 1991.

where the $M \times M$ matrix $\mathbf{C}^{\pm}$ is

$$\mathbf{C}^{\pm}_{m,m'} = \frac{\sin\left(2\pi(f_a \pm f_w)(m - m')dt\right)}{\pi(m - m')dt} \tag{2.12}$$

The M eigenvectors of this eigenvalue equation are the M M-component wavelets $\{w_m\}$ (Lilly and Park, 1995). We also retain signal phase information by forming complex wavelets from even and odd pairs of wavelets (Lilly and Park, 1995):

$$w_m = \frac{w_{even} + i w_{odd}}{\sqrt{2}} \tag{2.13}$$

(see Figure 2.10 for some of the wavelets we have calculated). The procedure of constructing wavelets and convolving with the data is repeated for each time increment in the data series and for each frequency band.

The eigenvectors comprise a set of orthogonal wavelets that depend on the target frequency, the bandwidth, and the size of the time window. Though the eigenvectors we have defined depend on the same parameters as a standard wavelet, they do not constitute exactly self-similar versions of a prototype; however, they can be made to approach self-similarity if p and p_a are fixed and M is large. Numerical spline approximations to these functions are in fact self-similar (Lilly and Park, 1995). Hence, in principal, we generate this type of wavelet in the same way we create an optimal multi-taper function, only we parameterize it differently. Moreover, as defined above, our wavelets are not only time-limited and nearly band-limited, but also orthogonal and therefore statistically-independent transforms, permitting spectral averaging and hence reduced variance. We have not, however, been forced to increase the size of f_w or of ΔT in order to achieve this reduction in variance (Lilly and Park, 1995). Furthermore, by including both negative and positive frequency intervals in the energy minimization condition, we have minimized the contributions of overlapping— and hence non-orthogonal—sidelobes belonging to the leakier wavelets, i.e., we have minimized bias, which bounds typical multitaper transforms (Lilly and Park, 1995; Riedel and Sidorenko, 1995). Only a subset of the wavelets will guarantee good energy confinement. Since this approach includes negative frequency intervals, $\Delta f = 4f_w$, and about the first $L = \Delta f \Delta T = 4f_w \Delta T = 4p$ wavelet transforms will have energy concentrated in the bandwidth. Therefore, we form data transforms with the L wavelets that preserve adequate time-bandwidth confinement and form a vector from these L transforms:

$$S_{m'} = \sum_{m} w_m^{m'} s_{b-m} \tag{2.14}$$

$$G = \begin{pmatrix} s_{m'=0} \\ \cdot \\ \cdot \\ \cdot \\ \cdot \\ s_{m'=L-1} \end{pmatrix} \tag{2.15}$$

We estimate the spectrum Π by averaging the inner product of the L-component vector G (Lilly et al):

$$\Pi = 2\frac{G^\dagger(f_c,t) \bullet G(f_c,t)}{L} \tag{2.16}$$

2.5 The seismic data set

For this study we employed two seismic data sets: one from a temporary seismic array set up in the Black Thunder mining region of eastern Wyoming, and the other from the BAY (Bayanaul) and KKL (Karkaralinsk) stations of the NRDC seismic network in Kazakhstan (see Figures 2.11 and 2.12). The Wyoming data are three-component recordings of velocity?? taken by surface instruments?? at a sampling rate of 1/100 *sps*. The corner frequency is .0083 *hz*. The local geology is characterized by . The NRDC data are also three-component recordings of velocity made by surface and borehole instruments at a sampling rate of 1/250 *sps*, the surface instruments with a flat response down to 1 *hz* and the borehole with a flat response down to .2 *hz*. This area of Kazakhstan is seismically quiet and tectonically stable, and the instruments situated on granitic outcrops to reduce reverberations (Hedlin, 1991).

The 1996 Wyoming experiment was conducted explicitly to gather regional three-component array recordings of known quarry blasts detonated at the Black Thunder coal mine. This data set provides a generous set of ripple-fired mining recordings at a variety of azimuths encircling the events (see Figure 2.11). Here we have analyzed the data taken on July 19 of a quarry blast consisting of a total of 620 shots arranged in 7 rows and interdelayed by about 35 *ms*. The data from the BAY and KKL stations of the NRDC network were chosen because they are three-component recordings of known single-shot and ripple-fired mining explosions at a local quarry and have a good signal-to-noise ratio. We include in our analyses a known ripple-fired event (day 135 of the 1987 recordings) and 20 ton single-shot mining calibration explosion known as Chemex 2 (day 245 of the 1987 recordings) so as to compare recordings of single and ripple-fired source types in the same region and at the same stations. Though differing regional geologies and specific mining practices present drawbacks for comparisons between the two data sets, their similar source-to-receiver range presents one advantage. We require three-component data in all cases in order to perform the polarization calculations, and we desire recordings at different azimuths in order to
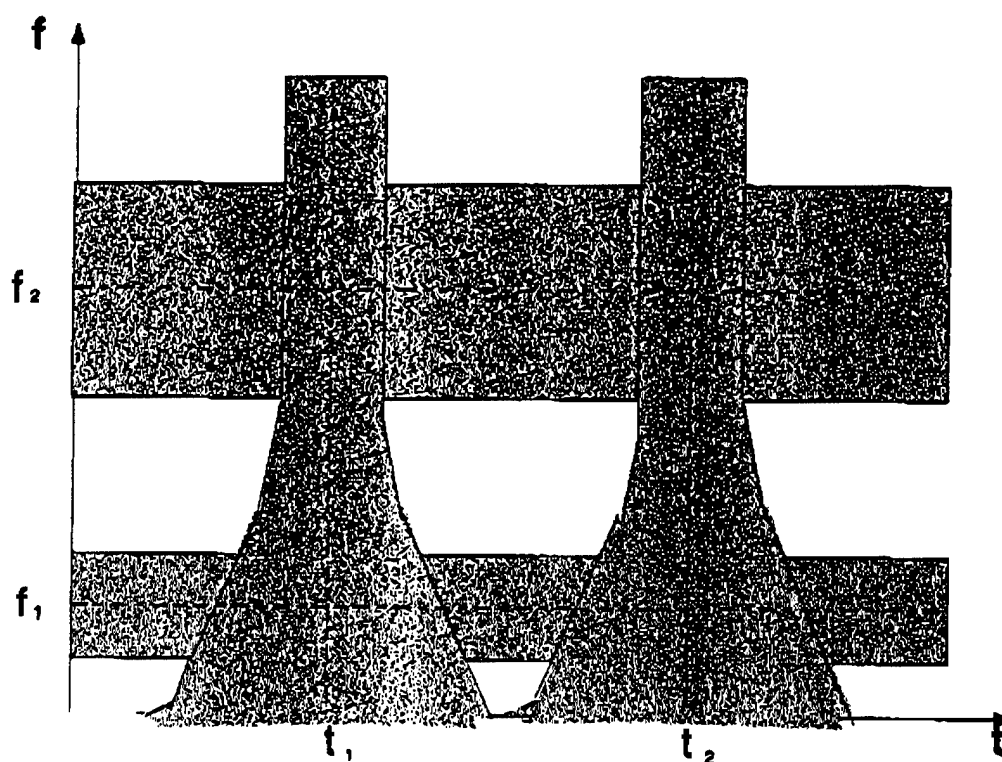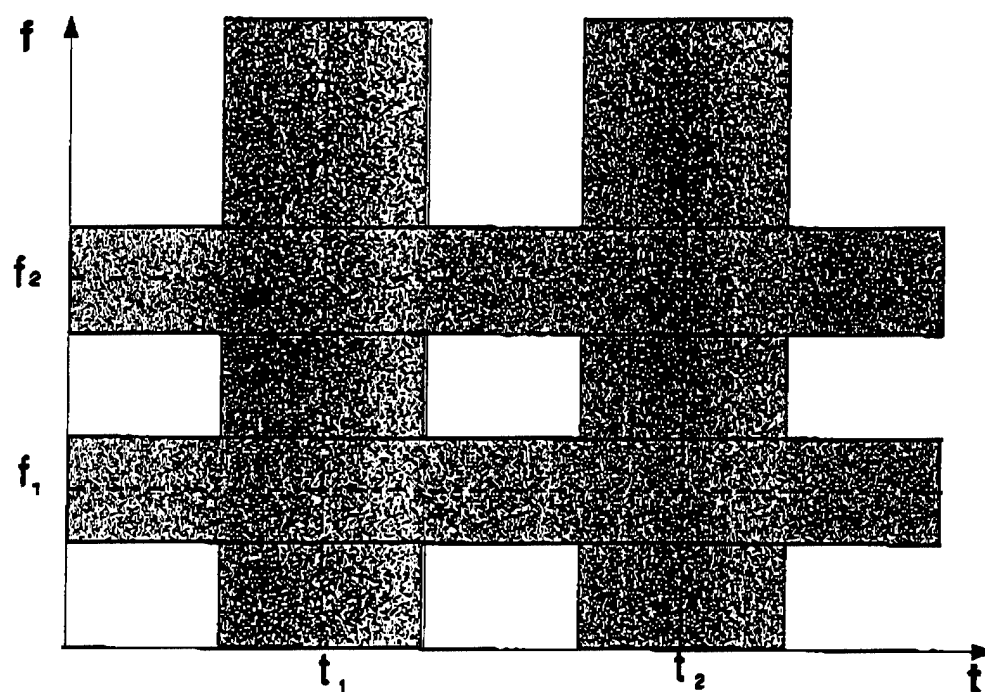
Figure 2.9 Fourier and wavelet decompositions are applied to the function $\delta(t - t_1) +$
$\delta(t - t_2) + exp(i2\pi f_1 t) + exp(i2\pi f_2 t)$, which in effect images the resolving power of the
transform in both the time and frequency domains; the Fourier spectrum is pictured above,
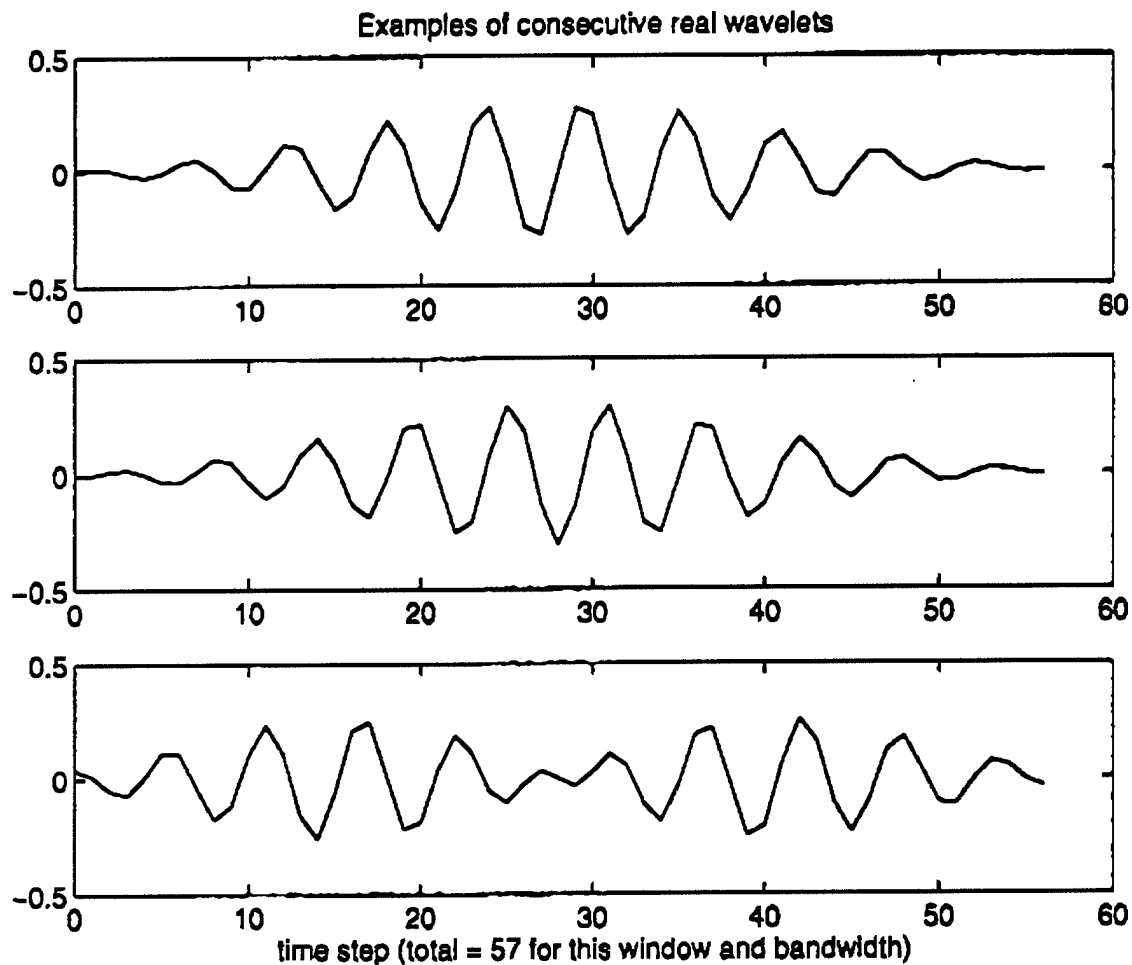
Examples of consecutive real wavelets

time step (total = 57 for this window and bandwidth)

Figure 2.10 An example of three consecutive, real wavelets. Note their alternating even and odd symmetry and that these have not been interpolated.

observe the azimuthal dependence, if any, of spectral characteristics, such as frequency dependence and time-independent banding. Before any of the data are analyzed, the three orthogonal time series are first rotated into an orthogonal radial-transverse-vertical coordinate system defined by the ray path of the signal (radial along the dirction of the ray path, transverse perpendicular to the ray path and parallel to the earth's surface, and vertical perpendicular to the earth's surface). The analysis at low frequencies benefits from first filtering and decimating the data. Both the NRDC and the Wyoming data have been decimated to 1 point in 25. The NRDC data have been low-pass filtered below 2 hz, and the Wyoming data below 1 hz, in both cases using a 1 hz lowpass convolution filter. Important geological parameters, such as local crustal depths, densities, etc., are summarized in Table 1.1.

2.6 A comparison

station	H	ρ	α	β
	km	gm/cm^3	km/s	km/s
Wyoming	39	2.85	6.30	3.56
NRDC	41	2.90	6.48	3.65

1.1 Average crustal parameters

Figures 2.13 and 2.14 display the spectral resolution characteristics at high frequency ranges of the multitaper and wavelet transforms, respectively. The wavelet transforms were computed using $p_c = 9.0$ and $p = 2.5$ to favor frequency resolution as much as possible over the wide range of frequencies under consideration. It is important to note when observing these figures that Figure 2.14 examines a smaller subsection of Figure 2.13. The wavelet transforms were computed using $p_c = 9.0$ and $p = 2.5$ to favor frequency resolution as much as possible over the wide range of frequencies under consideration without compromising excellent time resolution. The multitaper transforms were computed using 15 s windows and $p = 4.0$. At these parameter values, the wavelets drastically improve time resolution at all times, the accuracy being of course worst at the lowest frequencies analyzed. The wavelet frequency resolution may appear to be worse than the multitaper frequency resolution, but I believe it is in fact not worse. It only appears to be inferior because it is poor relative to the excellent time resolution, whereas the ratio of frequency resolution to time resolution in the multitaper spectrum is much closer to one. Therefore, at this value of p_c, the wavelets do not improve the frequency resolution achieved with multitapers, though at this value of p they do improve the time resolution. Figure 2.15 displays the wavelet spectrum of the same data calculated with the same value of p but with $p_c = 25.0$. The frequency resolution shows considerable improvement over its previous values, and finally appears to be on a par with the time resolution. However, such high values for p_c enforce prohibitively large and time-consuming calculations at the low frequencies (below 4 hz) that we examine in this study. The choice $p_c = 9$ appears to be about the limit to which we can stretch our demands given the numerical constraints imposed by low-frequency calculations using the Matlab software. It is interesting that, though the time-independent banding is still observed with improved time resolution, it is less pronounced. Multitapers may therefore prove advantageous if a visual recognition of this pattern is desired. The multitapers give better frequency resolution at high frequencies, and wavelets at low frequencies. Likewise, at the lowest frequencies, the multitaper resolution is almost on a par with the wavelet resolution. This suggests that wavelets are advantageous for frequency-dependent analyses at lower frequencies, and multitapers are perhaps still adequate for time-dependent localization and separation at lower frequencies and that in this case a multi-pronged approach may be optimal.

Chapter 3

Wavelet Polarization Analysis

3.1 Wavelet singular-value decomposition

Complex-valued wavelets give a means of evaluating a wave's polarization from the relative phases of its components recorded along three orthogonal seismometer axes. Polarization places constraints on the sometimes messy job of identifying phases present in the coda, most challenging in regional data with closely-spaced arrivals and scattering (Gal'perin, 1984). For example, only S waves can be circularly or elliptically polarized, and Rayleigh surface waves will be elliptically polarized until the P component attenuates, when it becomes vertically linearly polarized (Gubbins, 72; 1990). Also, the polarization angle of S waves relates to parameters entering the description of S radiation patterns (Kasahara, 45; 1981), which could tell us something about the type of source. Furthermore, when presented as a function of frequency and time in tandem with a sonogram, the polarization helps to visually locate patterns in energetic arrivals due to such factors as dispersion, scattering, and noise, and to spell out an arrival's region and distribution of influence in both time and frequency.

To estimate the principal polarization vector (for each time and frequency point), we first form a matrix S from the three seismometer component column vectors whose elements are the less leaky wavelet transforms (i.e., from the column vectors G that correspond to each seismometer component):

$$S = \begin{pmatrix} s_{0,1} & s_{0,2} & s_{0,3} \\ \cdot & \cdot & \cdot \\ \cdot & \cdot & \cdot \\ \cdot & \cdot & \cdot \\ \cdot & \cdot & \cdot \\ s_{L-1,1} & s_{L-1,2} & s_{L-1,3} \end{pmatrix} = (G_1 \quad G_2 \quad G_3)$$

where we have L transforms with good leakage properties. If we apply the singular value decomposition

(SVD) to the matrix S, we can approximate the principal polarization vector for certain regions of the time-frequency plane (Lilly and Park, 1995). The SVD breaks S down into a product of three matrices, the first and last of which will now be square and unitary:

$$S = U E V^\dagger \tag{3.1}$$

The first three column vectors, u_1, u_2, and u_3 of U are orthonormal eigenvectors of $SS^\dagger$, the first three column vectors of V are the eigenvectors of $S^\dagger S$, and the first three singular values of the diagonal matrix E are the corresponding eigenvalues (Strang, appendix; 1988). U is $L x L$, E is $L x 3$, and V is $3 x 3$. Because the first three columns of U are eigenvectors of $SS^\dagger$, they are, in effect, spectral estimates along the wave's principal axes of motion. Rotating S by a certain matrix R gives these spectral estimates weighted by the eigenvalues:

$$SR = (\sigma_1 u_1 \quad \sigma_2 u_2 \quad \sigma_3 u_3) \tag{3.2}$$

But this matrix R is none other than V itself (since V is unitary), which means that the columns of V contain the direction cosines between the principal axes of motion (i.e., of wave disturbance, not necessarily of propagation) and the seismometer axes. Furthermore, if $\sigma_1 \gg \sigma_2, \sigma_3$, then most of the motion occurs along $\sigma_1 u_1$, in which case v_1 denotes the principal polarization vector (Lilly and Park, 1995). These polarization estimates are good, however, only for certain regions of the time-frequency plane, since they are predicated upon a relatively large first singular value, a condition satisfied only in certain regions. It is possible to assess their validity by calculating and plotting confidence estimates of the first singular value based on Monte Carlo simulations of the SVD (Lilly and Park, 1995).

3.2 Results for synthetic data

The accuracy and power of the polarization calculations is tested on three synthetic cases whose expected polarizations are known: a two-component, completely in-phase sinusoidal pulse, a two-component ninety degree out-of-phase sinusoid, and a single-component chirp signal, with a small dose (3 % of the maximum signal) of random noise added in all cases (see Figures 3.1 through 3.8). The noise is added to strengthen the test, for we expect to see random polarizations over time and frequency bandwidths containing noise and coherent polarization over time and frequency regions containing predominantly coherent signal. Clearly in the first case (Figures 3.1 through 3.3), we expect, over the time and frequency range of the energy, a linearly-polarized signal oriented at a 45 degree angle to both orthogonal components, and random
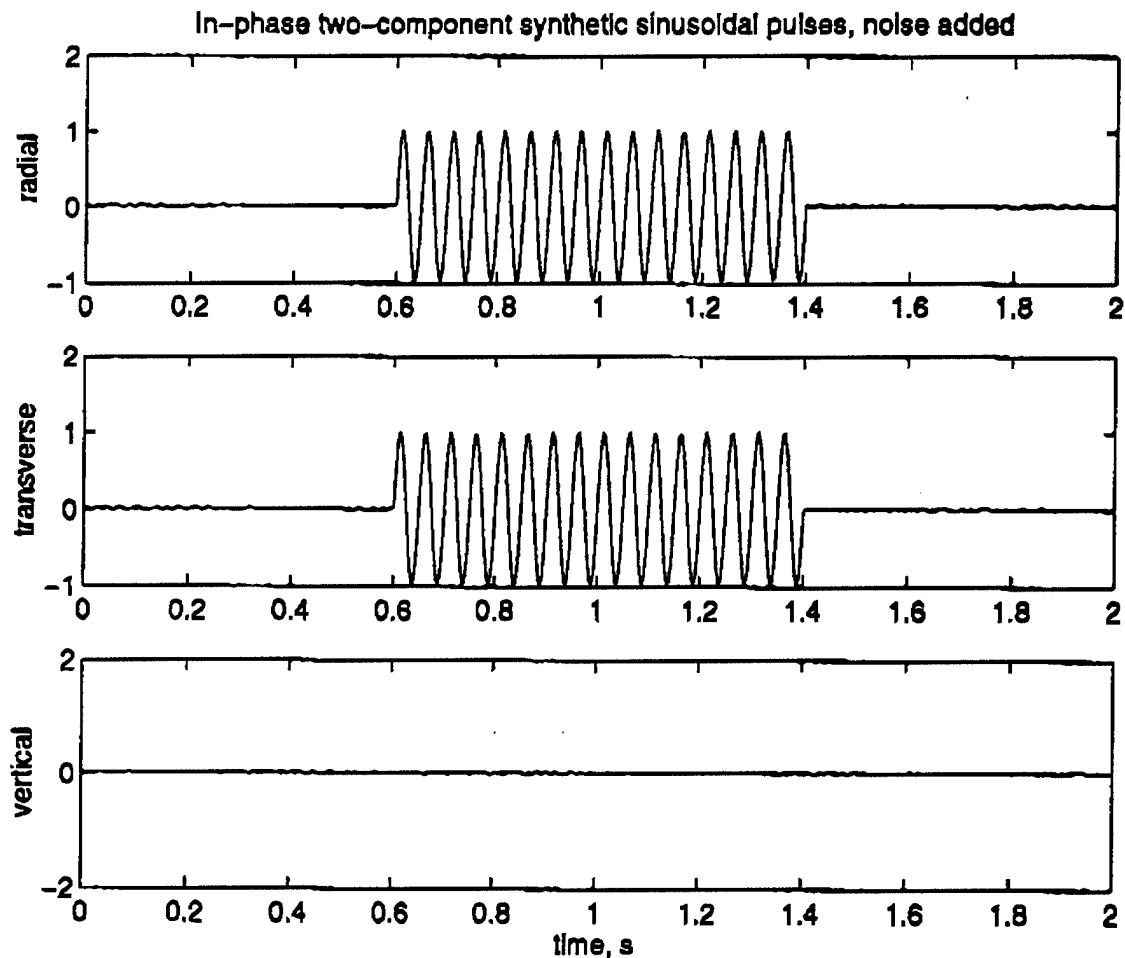
Figure 3.1 The two-component signal corresponding to a noisy sinusoidal pulse linearly-polarized in the transverse-radial plane along with pure noise along the third, vertical direction.

polarization due to noise elsewhere. In the second case (Figures 3.4 through 3.6) we expect a circularly-polarized signal over the time and frequency intervals coincident with coherent energy, and again random polarization elsewhere. For the chirp input (Figures 3.7 through 3.8) we expect a dispersive spectrum with linear polarization over regions of significant energy, and randomly-polarized noise everywhere else. This is indeed what we observe in all cases as Figures 3.7 and 3.8 illustrate. The grid of lines or circles appearing over small time and frequency bands and superimposed upon the spectrum represent the signal polarization for the given time and frequency band. The component of polarization that lies parallel to the horizontal axis represents the radial component, and that parallel to the vertical axis represents either the transverse or the vertical signal, as noted in each case. The polarization locks right onto the expected orientations over energetic times and frequencies and remains random over regions of pure noise.

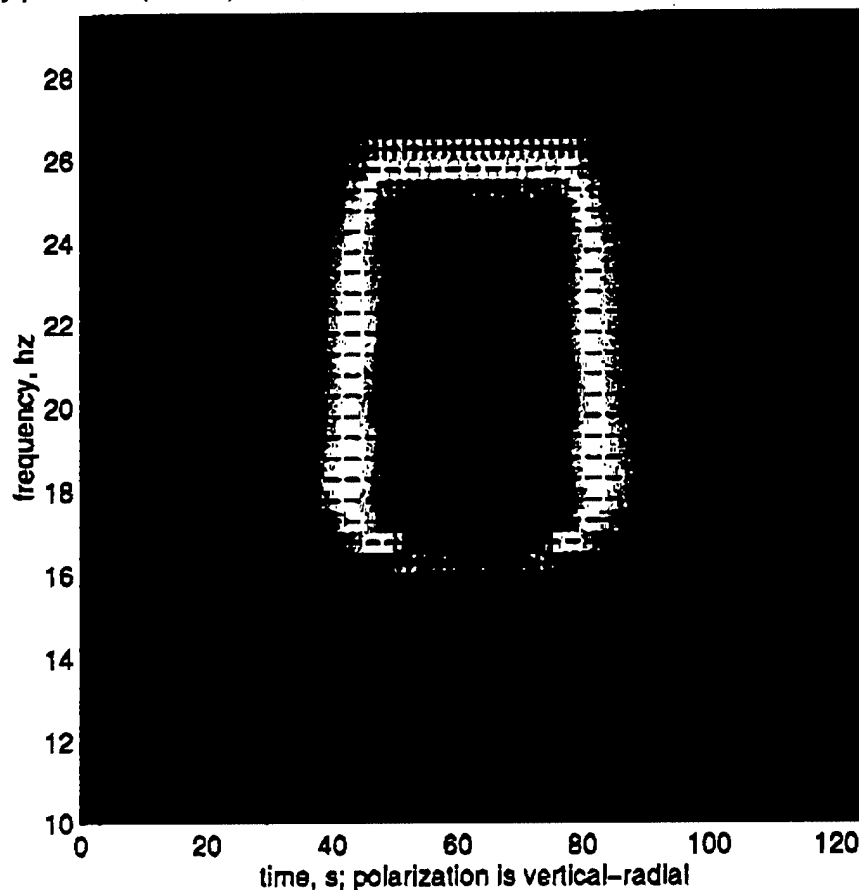Linearly polarized (i.e., in phase) two-component synthetic sinusoidal pulse with noise added

Figure 3.2 The vertical-radial polarization superimposed on the radial spectrum of the pulse in the last figure; note that the polarization is denoted by the superposed magenta curves, with the radial component always plotted along the horizontal axis; the spectrum amplitude corresponds to the color in the time-frequency plane.

3.3 Identification of surface wave phases using polarization

Figures 3.9 and 3.10 show the .05 to 1 hz sonogram spectrum and polarization (indicated by the overlying purple circles, lines, and dots) of a ripple-fired quarry blast at the station LBOH in Wyoming. Figure 3.9 displays the vertical-radial polarization (radial component along the horizontal axis, vertical along the vertical axis) overlying the vertical spectrum, while Figure 3.10 displays the transverse-radial polarization (now the transverse component along the vertical axis) with the transverse spectrum. These results provide a good example of the power of the polarization calculation to determine possible identifications of energetic

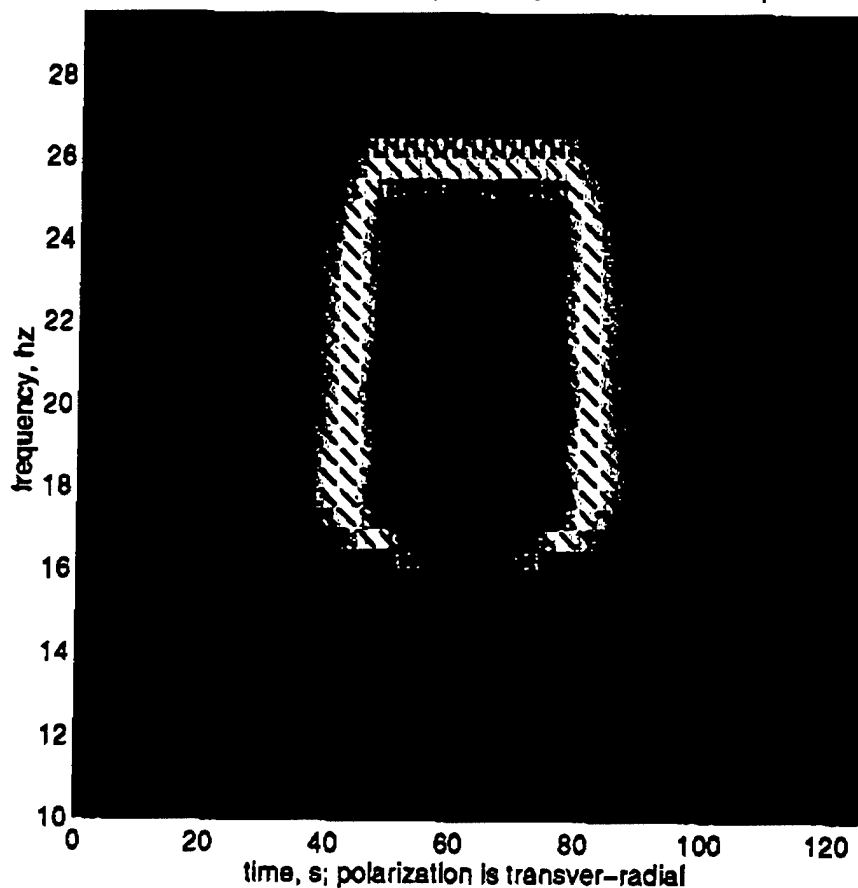Linearly polarized (i.e., in-phase) two-component synthetic sinusoidal pulse with noise added

Figure 3.3 The transverse-radial polarization of the linearly-polarized pulse over the radial (or, equivalently, the transverse) spectrum; random noise corresponds to random polarization where the siganl is insignificant.

components. The ambiguity present in the arrival times of different phases, complicated by dispersion, would make it difficult to identify them. It also provides a much more accessible means of identifying phases and their group velocities than performing the commonly-used Multiple Filter Analysis proposed by Dziewonski, et al. (1969). Without the polarization information, one might be tempted to ascribe the earliest-arriving energy to SH surface waves, since such surface energy typically travels faster than that of P-SV surface waves. But in fact we see with the aid of the polarization curves that the SH energy arrives simultaneously with that of P-SV, and, though generally sandwiched at frequencies below it, overlaps it to some extent. To distinguish the transverse and vertical components of spectra overlapping one another in the time-frequency plane would be difficult from the spectra alone. Moreover, though multi-component spectra may pinpoint regions of, say, simultaneous vertical and radial energy, they cannot tell us whether the energy
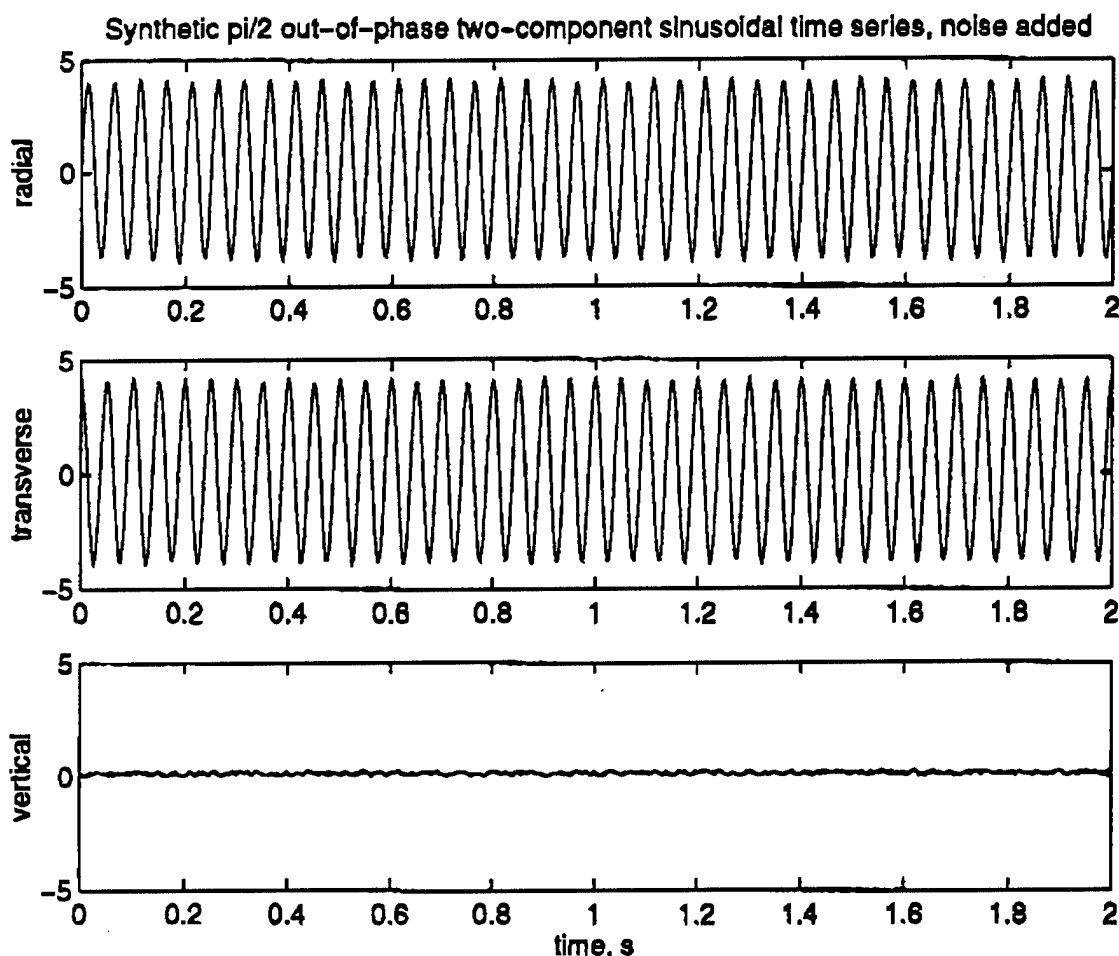
Synthetic pi/2 out-of-phase two-component sinusoidal time series, noise added

Figure 3.4 The two-component time series of a synthetic noisy circularly polarized sinusoidal signal along the radial and transverse directions with pure noise along the third, vertical direction.

is elliptically or linearly polarized, and, in either case, at which angle. These are also very important pieces of information for phase identification. We would, for example, expect a Rayleigh wave to be elliptically polarized, and we might find, as another example, that a particular polarization angle conveys information about the direction of force at the source, or, alternatively if this direction is known, the source-to-receiver azimuth (see Gal'perin, 1984, and Kasahara, 1981).

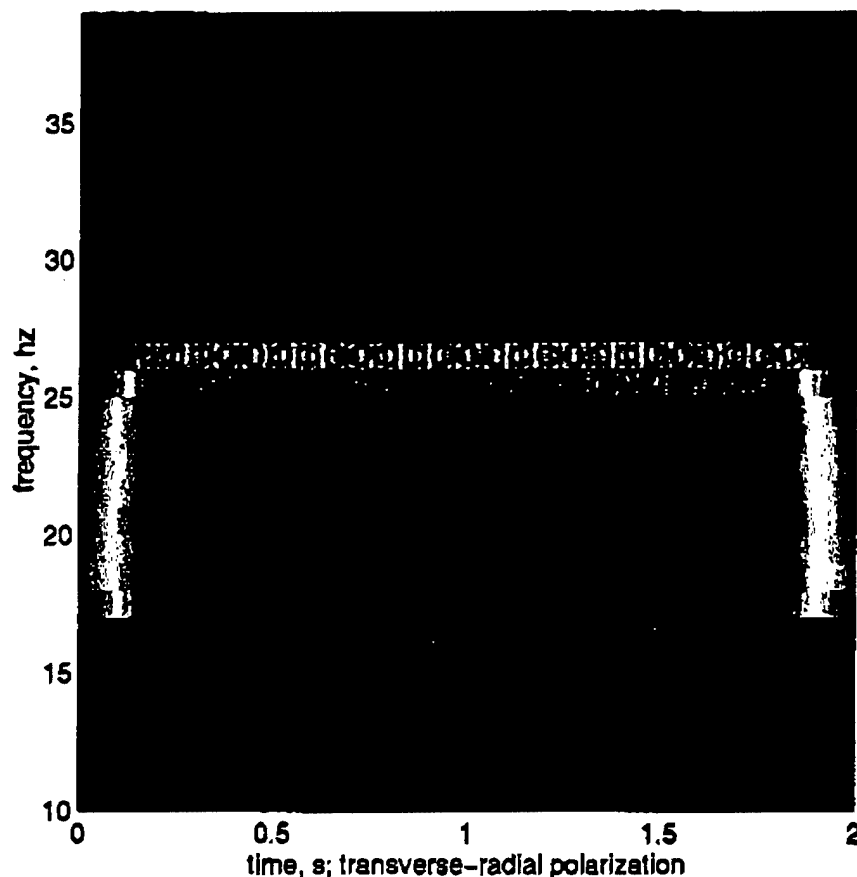Synthetic circularly-polarized (i.e., pi/2 out-of-phase) two-component signal with noise added

Figure 3.5 The transverse-radial polarization and the radial spectrum of the circularly polarized signal.

References

Dziewonski, A., S. Bloch, and M. Landisman, A techniquie for the analysis of transient seismic signals. *Bull. Seismol. Soc. Am.* , **59**, 427-444, 1969.

Flinn, E. A., Signal analysis using rectilinearity and direction of particle motion. Fifth paper in a series of six: Data processing techniques for the detection and interpretation of teleseismic signals. Archambeau, C. B. et al, ed.'s. *Proc. IEEE*, **53**, 1860-1884, 1965.

Gal'perin, E. I., *The Polarization Method of Seismic Exploration*. D. Reidel Publishing Company, Dordrecht, Holland, 1984.

Gubbins, David, *Seismology and Plate Tectonics*. Cambridge University Press, 1990.

Kasahara, K., *Earthquake Mechanics*. Cambridge University Press, 1981.

Lilly, Jonathen M. and Jeffrey Park, Multi-wavelet spectral and polarization analysis of seismic records. *Geophys. J. Int.* , **122**, 1001-1021, 1995.

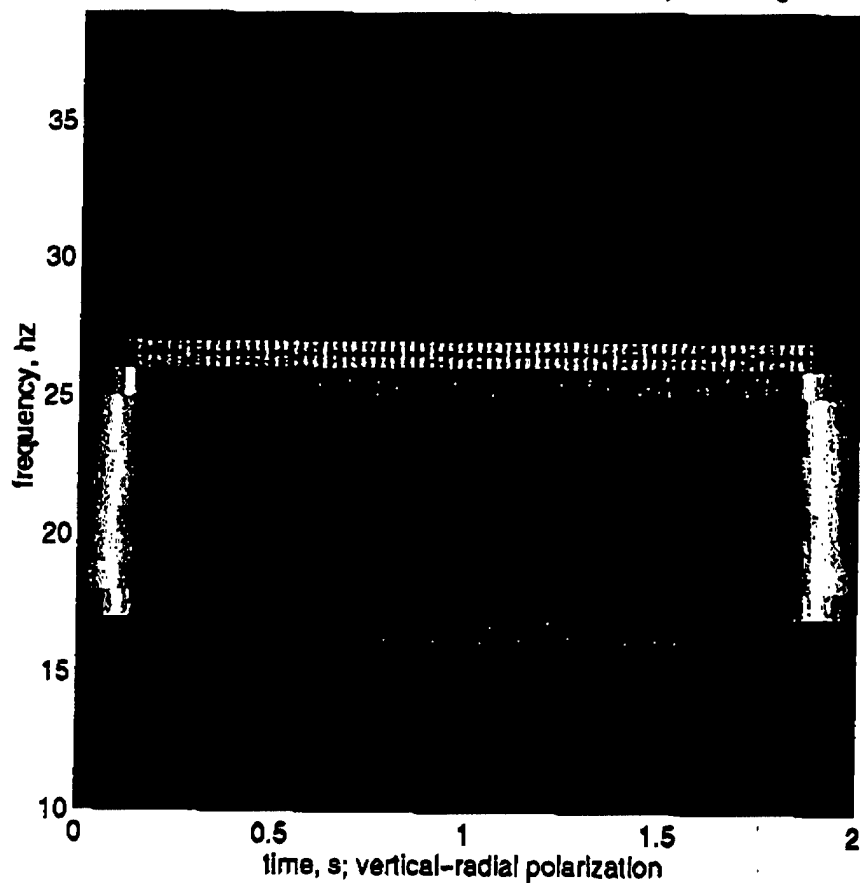Synthetic circularly-polarized (i.e., pi/2 out-of-phase) two-component signal with noise added

Figure 3.6 The vertical-radial polarization and radial spectrum of the circularly polarized signal.

Perelberg, Azik I. and Scott C. Hornbostel, Applications of seismic polarization analysis. *Geophysics*, 11, 671-676, 1994.

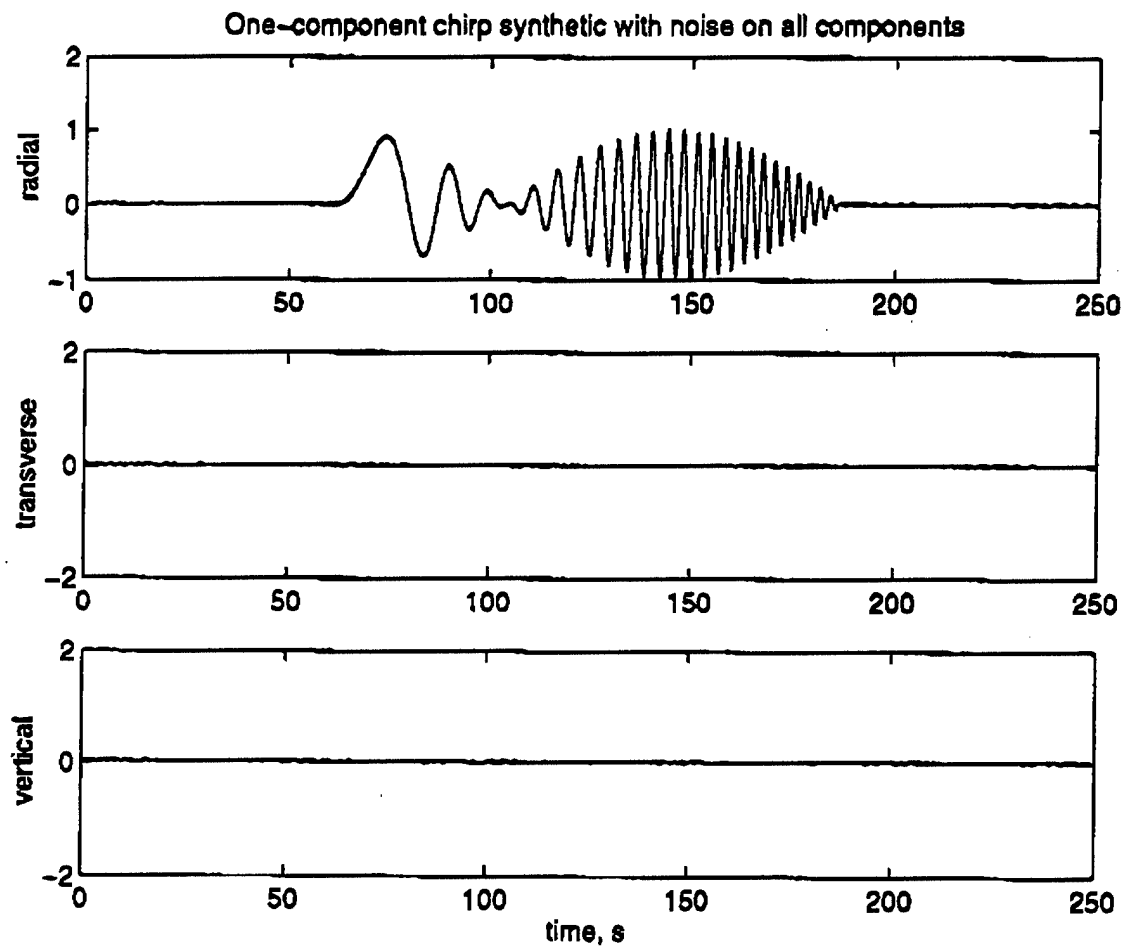Strang, Gilbert, *Linear Algebra and Its Applications*. Harcourt, Brace, Jovanovich, Inc., 1988.

One-component chirp synthetic with noise on all components

Figure 3.7 A synthetic one-dimensional chirp with noise added on all three components.

noisy radial chirp spectrum, with transverse–radial polarization
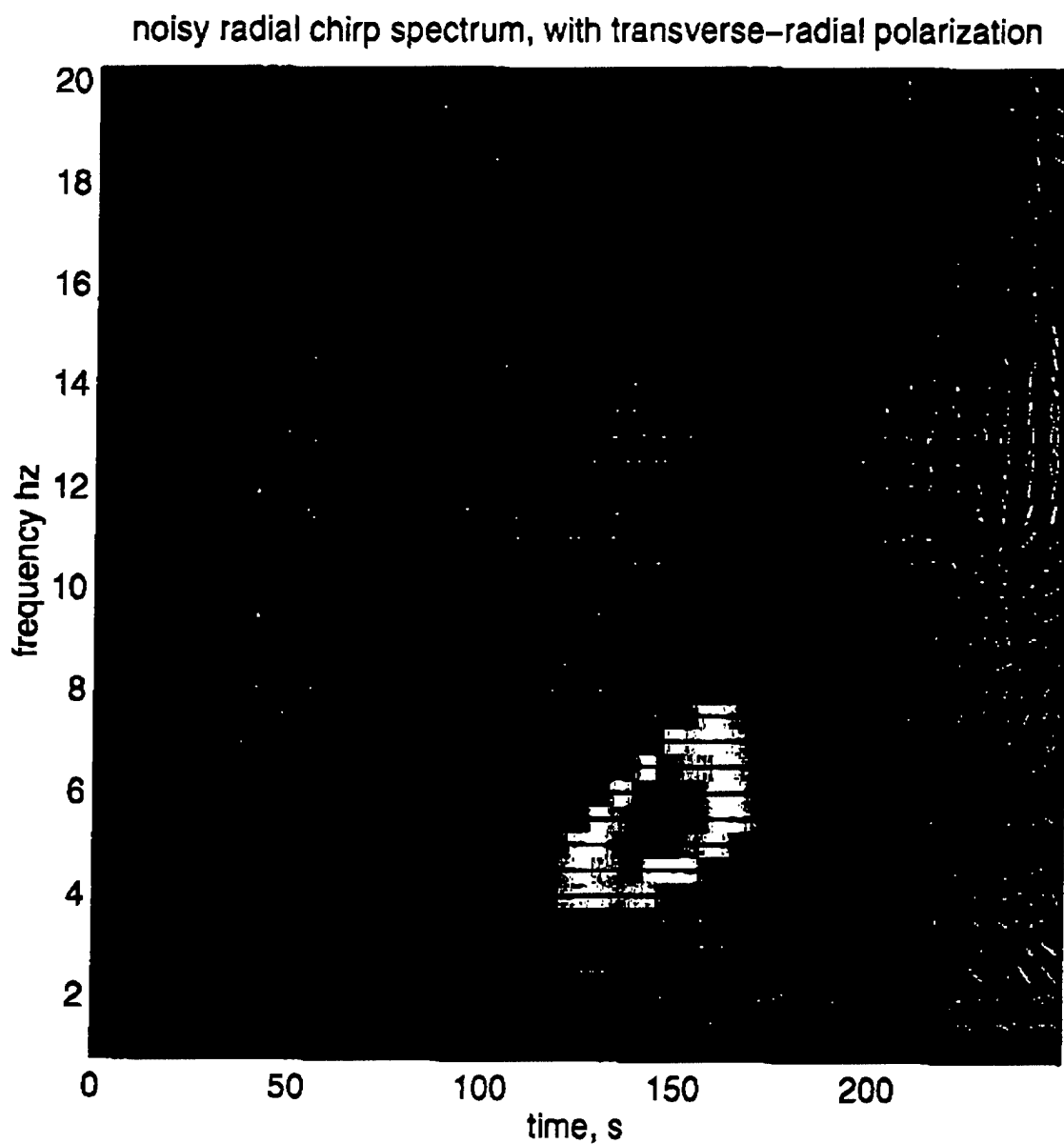

Figure 3.8 The transverse (or vertical)-radial polarization and radial spectrum of the noisy synthetic chirp signal.

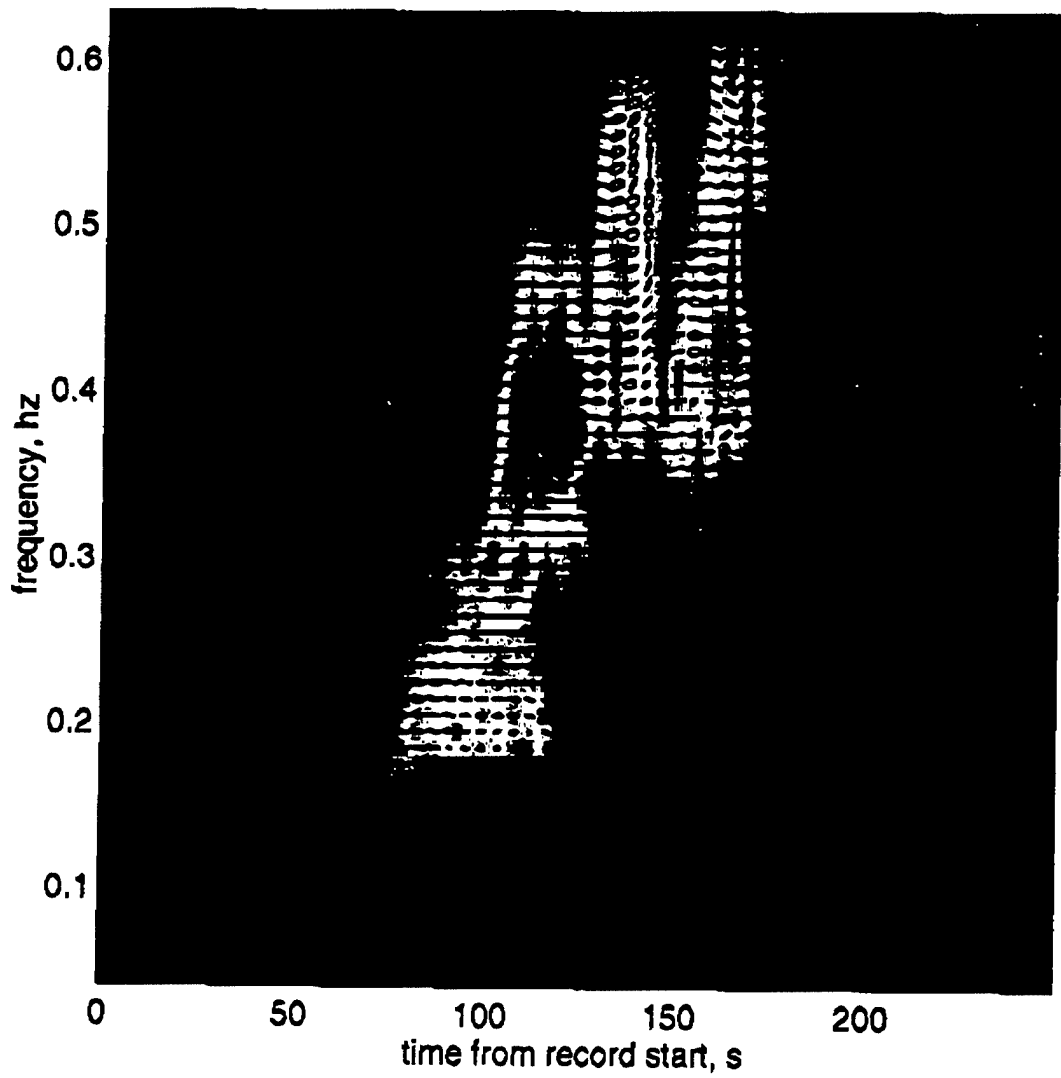July 19 1996, Wyoming, Iboh; vertical–radial polarization, vertical spectrum

Figure 3.9 The vertical-radial polarization and vertical spectrum of the ripple-fired event recorded in Wyoming by LBOH.

July 19 1996, Wyoming, Iboh; transverse–radial polarization, transverse spectrum

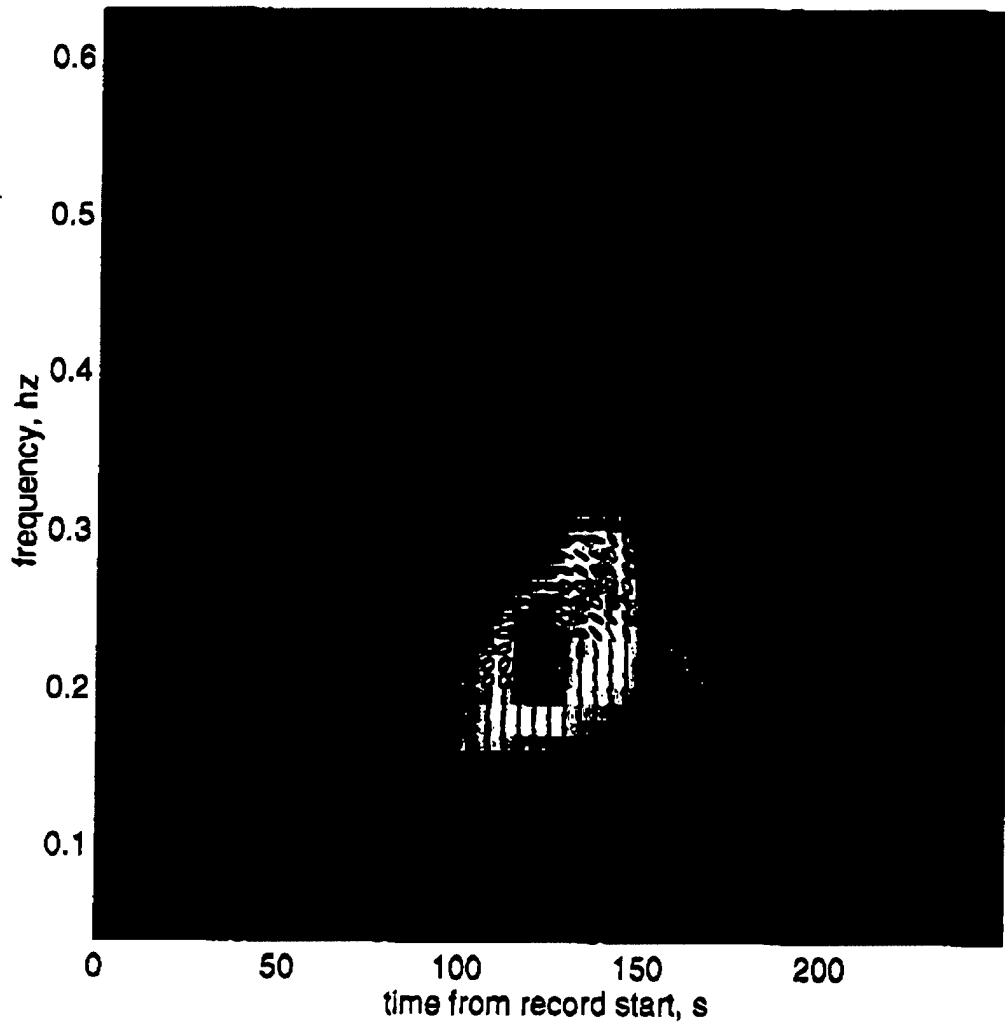**Figure 3.10** The transverse-radial polarization and transverse spectrum of the same event as the last figure, also recorded at LBOH.